Resonant production of light sterile neutrinos in compact binary merger remnants

Garðar Sigurðarson,[1] Irene Tamborra,[1] and Meng-Ru Wu[2,3]
[1]*Niels Bohr International Academy and DARK, Niels Bohr Institute, University of Copenhagen, Blegdamsvej 17, 2100 Copenhagen, Denmark*
[2]*Institute of Physics, Academia Sinica, Taipei 11529, Taiwan*
[3]*Institute of Astronomy and Astrophysics, Academia Sinica, Taipei 10617, Taiwan*

(Received 19 September 2022; accepted 12 December 2022; published 29 December 2022)

The existence of eV-mass sterile neutrinos is not ruled out because of persistent experimental anomalies. Upcoming multimessenger detections of neutron-star merger remnants could provide indirect constraints on the existence of these particles. We explore the active-sterile flavor conversion phenomenology in a two-flavor scenario (one active plus one sterile species) as a function of the sterile neutrino mixing parameters, the neutrino emission angle from the accretion torus, and the temporal evolution of the merger remnant. The torus geometry and the neutron richness of the remnant are responsible for the occurrence of multiple resonant active-sterile conversions. The number of resonances strongly depends on the neutrino emission direction above or inside the remnant torus and leads to a large production of sterile neutrinos (and no antineutrinos) in the proximity of the polar axis, as well as more sterile antineutrinos than neutrinos in the equatorial region. As the black-hole torus evolves in time, the shallower baryon density is responsible for more adiabatic flavor conversion, leading to larger regions of the mass-mixing parameter space being affected by flavor mixing. Our findings imply that the production of sterile states could have indirect implications on the disk cooling rate, its outflows, and related electromagnetic observables which remain to be assessed.

DOI: 10.1103/PhysRevD.106.123030

I. INTRODUCTION

The coalescence of a neutron star (NS) with another NS or a black hole (BH) leads to the formation of a compact binary merger. Compact binary mergers lose angular momentum through the emission of gravitational waves. This conjecture was recently confirmed through the detection of the gravitational-wave event GW170817 [1–8]. Electromagnetic follow-up observations across multiple wave bands of GW170817 confirmed that NS merger remnants are factories of the elements heavier than iron and harbor short gamma-ray bursts [9–14].

While no neutrino has yet been observed from gravitational-wave sources [15–17], thermal neutrinos are copiously produced in binary NS mergers, with the neutrino luminosities reaching up to 10^{54} erg/s within $\mathcal{O}(100)$ ms [18,19]. Neutrinos dominate the cooling of the NS merger remnant and affect the ejecta composition, while neutrino pair annihilation above the BH accretion disk contributes to power the short gamma-ray burst jet [18–28].

Despite intense work, the treatment of neutrino transport in hydrodynamical simulations of binary NS mergers is still approximated because of the technical challenges linked to the required three-dimensional general-relativistic magnetohydrodynamical modeling of the source. In addition, neutrinos are treated as radiation, with the occurrence of flavor conversion neglected. However, the protonization of the merger remnant (i.e., the excess of electron antineutrinos with respect to electron neutrinos) presumably leads to the occurrence of the matter-neutrino resonance due to the cancellation of the matter potential involving interactions of neutrinos with electrons and the neutrino-neutrino potential [29–35]. Recent work has focused on exploring the implications of $\nu - \nu$ interactions on the synthesis of the elements heavier than iron in the neutrino-driven outflow and the physics of neutrino-cooled accretion disks [36–42].

The expected large number of binary NS merger remnant observations will offer unprecedented opportunities to characterize the population of binary NS mergers, as well as the physics of NSs and their nuclear equations of state [43–46]. At the same time, upcoming multimessenger observations of binary NS merger remnants and short gamma-ray bursts could provide constraints on physics beyond the Standard Model, see, e.g., Refs. [47–49] for some examples. An interesting and unexplored scenario in this regard concerns extra sterile neutrino families with eV mass [50,51].

The existence of sterile families of neutrinos has not yet been confirmed. However, to date, it is challenging to interpret a number of experimental results within the standard three neutrino flavor framework [52,53]. Earlier hints on the existence of a fourth sterile neutrino family were provided by the LSND Collaboration experiment and partly confirmed by MiniBooNE [54,55]. Along the same lines, reactor neutrino data could have been explained by invoking the existence of an eV-mass sterile neutrino; these puzzling effects concerning reactor neutrino fluxes now seem to be fully understood [56–60], despite remaining uncertainties on the reactor energy spectra [61,62]. Additional anomalies were also found by the Gallium experiments GALLEX and SAGE [63] and were recently confirmed by the Baksan Experiment on Sterile Transitions [64,65]. As a consequence, global fits invoking the existence of extra sterile neutrino families easily accommodate some datasets but are somewhat in tension with others [66–68]. Cosmological data do not rule out the existence of light sterile neutrinos [69–72]. We refer the interested reader to Refs. [50,52,53] for recent reviews on the topic and details on the best-fit mixing parameters preferred by the datasets quoted above.

The phenomenology of light sterile neutrinos in core-collapse supernovae (SNe) has been widely investigated; these particles could have an impact on the synthesis of the elements heavier than iron as well as on shock revival [73–77]. Their existence could also strongly affect the expected neutrino signal from the next galactic SN [78,79]. However, despite similarities in terms of neutrino number densities and energetics, the active-sterile flavor conversion physics and its indirect consequences on the multimessenger emission have not been explored in the context of binary NS mergers.

In this paper, we rely on the output from one of the binary remnant simulations of Ref. [23] and, for the first time, investigate the production of sterile particles from active states through resonant neutrino-matter interactions, and eventual reconversion into active states. Our work is organized as follows. In Sec. II, we introduce our benchmark binary NS merger remnant model and its main features. Section III focuses on the physics of active-sterile flavor conversions in binary NS merger remnants. The flavor conversion phenomenology is explored in Sec. IV as a function of the active-sterile mixing parameters, while the production of sterile particles as the BH torus evolves as a function of time is outlined in Sec. V. Finally, a summary of our findings is reported in Sec. VI.

II. BINARY NEUTRON STAR MERGER REMNANT MODEL

We rely on outputs of a 2D (hereafter, assumed equivalent to a 3D simulation carried out under the assumption of cylindrical symmetry) hydrodynamical simulation of the BH accretion torus formed in the postmerger phase of a compact binary merger. Specifically, we adopt the model M3A8m3a5 presented in Ref. [23], based on subgrid viscosity and neutrino moment transport, while neglecting the magnetic field modeling. This simulation is set up by relying on an idealized equilibrium torus around a central BH of $3M_{\odot}$; it has a dimensionless BH spin parameter of 0.8, and a torus of $0.3M_{\odot}$. The total mass of the neutrino-driven (mostly ejected at early times away from the equator) ejecta is $1.47\times10^{-3}M_{\odot}$, while the total outflow mass (driven outward also close to the equator and mostly determined by the viscously driven ejecta) is $66.2\times10^{-3}M_{\odot}$. We refer the interested reader to Ref. [23] for details on the simulation setup.

In this model, as the accretion torus forms, it starts to lose mass while accreting onto the central BH. During the first $\mathcal{O}(10)$ ms, the environment is optically thick and neutrino cooling is less efficient. As the density drops, it follows a phase of neutrino-dominated accretion flow, during which neutrino cooling balances viscous heating. As the mass and density of the torus decrease, the neutrino production rate is also reduced, until neutrino cooling is no longer efficient and the torus enters a phase dominated by advection during which the viscous heating drives the expansion of the torus and launches outflows.

Figure 1 illustrates the characteristic properties of our BH torus remnant model and displays the baryon mass density, the electron fraction as well as the ν_e number density, and the relative difference between the ν_e and $\bar{\nu}_e$ number densities in the region above the disk. All quantities have been extracted at 25 ms for representative purposes and are shown in the $x-z$ plane, under the assumption of cylindrical symmetry around the z axis. Note that in the following we track the flavor conversion physics along a radial direction r, defined such that $x=r\cos\theta$ and $z=r\sin\theta$, with θ being the polar angle measured with respect to the z axis.

One can see that $n_{\bar{\nu}_e}\simeq n_{\nu_e}$ in the polar region. However, as a function of time, the BH torus evolves from a configuration where $n_{\bar{\nu}_e}>n_{\nu_e}$ to one with $n_{\bar{\nu}_e}<n_{\nu_e}$ in the proximity of the polar axis [23,38]. On the other hand, nonelectron flavors of neutrinos and antineutrinos are thermally produced in small amounts but can be generated through flavor conversion [23].

At high densities, neutrinos are coupled to the matter background. As the matter density decreases, neutrinos decouple from matter and start to free stream. The neutrino energy distributions for the electron flavors follow Fermi-Dirac distributions with nonzero chemical potential in the trapping regime and then tend to become pinched in the free-streaming regime. In the numerical computations, we rely on the numerical energy densities provided as output of our benchmark NS merger model [23]. In order to assess whether the production of sterile particles occurs while the active neutrinos free stream, we estimate the location of the decoupling surfaces by requiring that the following condition is satisfied for the flux factor [38]

$$\frac{|\mathbf{F}_{\nu_e,\bar{\nu}_e}|}{n_{\nu_e,\bar{\nu}_e}}=\frac{1}{3}, \tag{1}$$

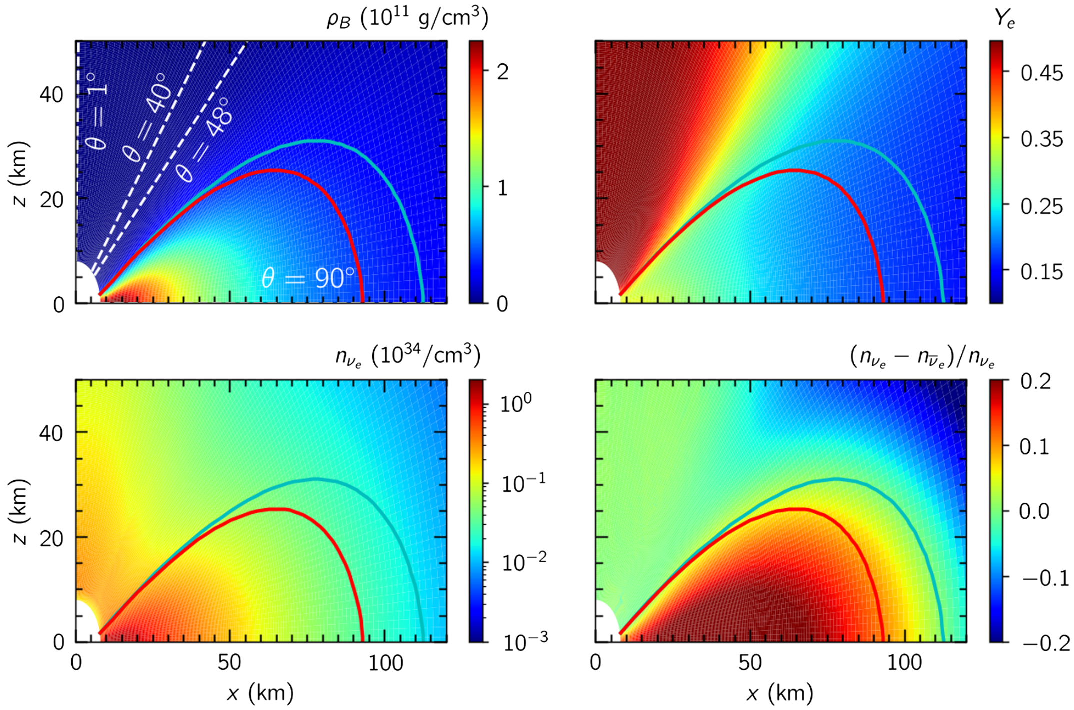

FIG. 1. Properties of the BH torus remnant at 25 ms in the plane spanned by x and z, under the assumption of cylindrical symmetry around the z axis: baryon mass density (top left panel), electron fraction (top right panel), number density of electron neutrinos (bottom left panel), and relative difference between electron neutrinos and antineutrinos (bottom right panel). The decoupling surfaces of ν_e and $\bar{\nu}_e$ are shown in blue and red, respectively [see Eq. (1)]. In the top left panel, our benchmark neutrino emission directions defined by $\theta = 1°$, 40°, 48°, and 90° are marked with dashed white lines.

where $\mathbf{F}_{\nu_e,\bar{\nu}_e}$ is the number flux and $n_{\nu_e,\bar{\nu}_e}$ is the number density of ν_e or $\bar{\nu}_e$ extracted from our benchmark hydrodynamical simulation.

Sterile particles could be produced in the collisional regime (see Sec. III); hence, we compute the mean free path for the main neutral current (NC) and charged current (CC) interactions (i.e., scattering of neutrinos on nucleons, neutrino-(anti)neutrino scattering, bremsstrahlung processes, and beta reactions) by following Refs. [80–85]:

$$\lambda_{\nu_e,\bar{\nu}_e}(E) = \frac{1}{\sum_{\mathrm{CC,NC}} n_t \sigma(E)}, \tag{2}$$

where $\sigma(E)$ is the interaction cross section and n_t the number density of targets. We assume that Pauli blocking effects are negligible, because the torus has a mass density much lower than the nuclear saturation density ($\rho_B \ll \mathcal{O}(10^{14})$ g/cm; see Fig. 1) and is only moderately degenerate for electrons (see, e.g., Fig. 1 of Ref. [38]).

III. ACTIVE-STERILE FLAVOR CONVERSION PHYSICS

In this section, we introduce the equations of motion describing the production of sterile particles. We then investigate the resonant production of sterile particles in NS merger remnants.

A. Neutrino equations of motion

For simplicity, in this paper, we work in the two-flavor basis (ν_e, ν_s) and focus on flavor conversion between electron and sterile flavors. In fact, the nonelectron flavors are produced through flavor mixing; however, we neglect flavor conversion among the active flavors. The latter is an approximation, in light of recent hints supporting evidence for the development of non-negligible fast neutrino conversion at high densities [36,86–89]. As shown in Ref. [74], the production of sterile flavors may further trigger flavor transformation in the active sector, repopulating it. Nevertheless, because of the numerical challenges involved in the modeling of neutrino self-interaction and since we rely on mass and mixing angles between the active and sterile sectors that are larger than the active sector mixing parameters, we aim to provide a first explorative glimpse on the production of sterile states in NS merger remnants. An improved modeling of the flavor conversion physics in the presence of sterile neutrinos is left to future work.

Under the assumption of stationarity, the evolution of the neutrino field in the flavor space is described by the Liouville equation [90]:

$$\partial_r \rho_E = -i[H_E, \rho_E] + \mathcal{C}(\rho_E, \bar{\rho}_E), \tag{3}$$

$$\partial_r \bar{\rho}_E = -i[\bar{H}_E, \bar{\rho}_E] + \bar{\mathcal{C}}(\rho_E, \bar{\rho}_E), \tag{4}$$

where, for each energy mode E, ρ_E is a 2×2 density matrix, whose diagonal terms are the neutrino number densities for each flavor: (n_{ν_e}, n_{ν_s}). The bar denotes antineutrino quantities. We assume that sterile neutrinos are generated through flavor conversion, i.e., the initial conditions of our ensemble are such that $\rho_E = \mathrm{diag}(n^0_{\nu_e}, 0)$ and $\bar{\rho}_E = \mathrm{diag}(n^0_{\bar{\nu}_e}, 0)$. The Hamiltonian is

$$H_E = H_{v,E} + H_m. \tag{5}$$

The vacuum term is a function of the active-sterile mixing angle θ_v and the vacuum frequency $\omega = \Delta m^2/2E$ (with $\Delta m^2 > 0$ being the mass-squared difference):

$$H_{v,E} = \omega \begin{pmatrix} -\cos 2\theta_v & \sin 2\theta_v \\ \sin 2\theta_v & \cos 2\theta_v \end{pmatrix}. \tag{6}$$

The vacuum term has opposite sign for neutrinos and antineutrinos. The matter term of the Hamiltonian takes into account the coherent forward scattering on matter,

$$H_m = \begin{pmatrix} \lambda & 0 \\ 0 & -\lambda \end{pmatrix}. \tag{7}$$

The effective matter potential is given by [73]

$$\lambda = \frac{\sqrt{2} G_F \rho_B}{2 m_N}(3Y_e - 1), \tag{8}$$

where G_F is the Fermi constant, ρ_B is the baryon mass density, m_N is the nucleon mass, and $Y_e = (n_{e^-} - n_{e^+})/n_B$ is the electron fraction. The terms $\mathcal{C}$ and $\bar{\mathcal{C}}$ in Eqs. (3) and (4) represent the collision terms due to the incoherent part of the scattering on the matter background.

Equations (3) and (4) assume that neutrinos propagate along radial directions (r) for simplicity, hence neglecting the neutrino angular distributions. In fact, while the contribution to the flavor conversion history from neutrinos traveling along nonradial directions should not be negligible, for this explorative work we expect the behavior along the radial direction to be representative of the flavor transformation phenomenology.

In dense regions, where the electron flavors are thermally produced, neutrino flavor conversion is suppressed because $\lambda \gg \omega$. As the matter density decreases, sterile flavors can be resonantly produced if the Mikheyev-Smirnov-Wolfenstein (MSW) resonance condition is satisfied [91–93]:

$$\lambda_{\rm res} = \pm \omega \cos 2\theta_v, \tag{9}$$

where the plus sign applies to neutrinos and the minus sign to antineutrinos.

To quantify the amount of flavor conversion at each resonance, we calculate the adiabaticity parameter γ at the resonance [94]:

$$\gamma = \frac{\omega}{\pi} \frac{\sin^2 2\theta_v}{\cos 2\theta_v} \left| \frac{d\lambda/dr}{\lambda} \right|^{-1}. \tag{10}$$

The corresponding transition probability at the resonance energy $E_{\rm res}$ is approximated by the Landau-Zener formula [94–96][1]:

$$P_{\nu_e \to \nu_s}(E_{\rm res}) \approx 1 - \exp\left(-\frac{\pi^2}{2}\gamma\right). \tag{11}$$

Resonant conversion between $\bar{\nu}_e$ and $\bar{\nu}_s$ occurs when $\lambda < 0$, i.e., $Y_e \lesssim 1/3$ [see Eq. (9)]. From Fig. 1, it thus becomes evident that $\bar{\nu}_s$'s cannot be produced around the polar region, since $Y_e \gtrsim 1/3$ there.

Sterile particles can also be produced collisionally [97]. However, for our benchmark NS merger remnant model and sterile mass-mixing parameters, we have verified that the collisional production of sterile (anti)neutrinos is always negligible. An analogous situation occurs in the SN context, where, however, keV-mass sterile states can be produced collisionally [84,85].

B. Active-sterile flavor conversion

We now intend to investigate the active-sterile flavor conversion phenomenology for our benchmark NS merger remnant model. Figure 2 shows the radial neutrino-matter forward scattering potential at $t = 25$ ms for representative radial directions with emission angles: $\theta = 1°$, $40°$, $48°$, and $90°$. The $\theta = 1°$ direction allows one to investigate the flavor conversion physics in the proximity of the polar region, and the corresponding λ is always positive. $\theta = 40°$ is representative of intermediate directions between the pole and the equator where λ is both positive and negative. The $\theta = 48°$ potential represents intermediate directions along which λ changes sign multiple times, while the $\theta = 90°$ potential shows the typical radial evolution of λ in the proximity of the equator. Our representative radial directions are chosen to highlight the strong dependence of the flavor conversion phenomenology on the emission angle. All other directions in between these ones have similar features. This is true even though some of our selected radial trajectories originate from regions outside the decoupling sphere. For instance, most trajectories originating from the neutrinosphere will eventually evolve outward nearly radially at large radii and undergo flavor transformation similar to one of our representative radial directions. The magnitude

[1]Note that, for our cases of interest, $|\lambda| \gg |\omega|$; however, if $\lambda \to 0$, Eq. (11) holds for $\theta_v \ll 1$ [95].

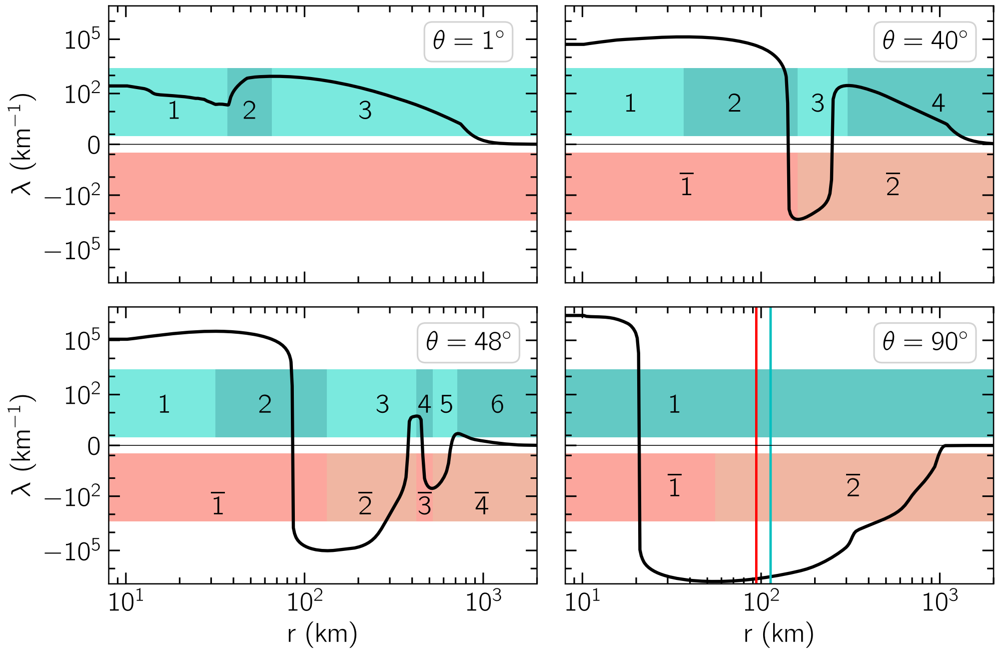

FIG. 2. Effective matter potential λ, extracted at $t = 25$ ms, as a function of the radius for our selected radial directions with emission angles: $\theta = 1°$, $40°$, $48°$, and $90°$, from the top left panel to the right bottom panel, respectively (see Fig. 1). The green and red bands show $\lambda_{\rm res}$ for $(\sin^2\theta_v, \Delta m^2) = (10^{-2}, 10^{-1}\ \mathrm{eV}^2)$ and $E \in [0.1, 300]$ MeV for neutrinos and antineutrinos, respectively. Owing to the geometry of the torus, the shape and magnitude of λ greatly vary as functions of θ, and so do the resonance regions. For each θ, the number of MSW resonances occurring for neutrinos and antineutrinos is marked by different hues. Each resonance is identified through the change of sign of $d\lambda/dr$. For $\theta = 90°$, the neutrino and antineutrino decoupling surfaces are plotted as vertical lines in blue and red, respectively. The radial directions $\theta = 1°$, $40°$, and $48°$ fall outside the decoupling surfaces.

of λ is the highest around the equatorial plane (see the bottom right panel) and drops toward the polar axis (see the top left panel); see also Eq. (8) and Fig. 1.

For $(\sin^2\theta_v, \Delta m^2) = (10^{-2}, 10^{-1}\ \mathrm{eV}^2)$ and $E \in [0.1, 300]$ MeV, we can see from Fig. 2 that (anti)neutrinos undergo multiple resonances because of the spatial variations of Y_e and ρ_B, as shown in Fig. 1. In order for the MSW resonance to occur, the neutrino mean free path [Eq. (2)] has to be larger than the resonance width,

$$\Delta_{\rm res} = \tan 2\theta_v \left|\frac{d\lambda/dr}{\lambda}\right|^{-1}. \tag{12}$$

We have verified that this is always the case for all scenarios considered in this work.

For the emission directions with $\theta = 1°$, $40°$ and $\theta = 48°$, the first resonance occurs outside the decoupling surfaces (see Fig. 2), where the production of ν_e's and $\bar{\nu}_e$'s has essentially stopped and the active flavors have entered the free-streaming regime. This implies that a large production of sterile particles may deplete the active sector (which is not repopulated through thermal processes), with implications for the electron abundance. On the other hand, for the $\theta = 90°$ direction, the first resonance occurs deep inside in the torus, where ν_e's and $\bar{\nu}_e$'s are still being thermally produced. As a consequence, although flavor conversion at the first resonance may not significantly impact the local number density of ν_e and $\bar{\nu}_e$, quickly replenished through thermal processes, it can potentially affect the evolution of the disk. Moreover, for $\theta = 90°$, neutrinos undergo MSW resonances before decoupling, which means that not all neutrinos cross the MSW resonances in the forward direction; yet, neglecting the backward moving neutrinos should have negligible implications on our qualitative assessment of the impact of the production of sterile states (see in the following and the discussion in Sec. IV).

In order to evaluate the amount of flavor transformation numerically, we introduce the ν_e survival probability at the resonance radius r_i:

$$P_{\nu_e\to\nu_e}(E, r_i) = \frac{n_{\nu_e}(E, r_i)}{n^0_{\nu_e}(E, r_i)}, \tag{13}$$

where the index 0 denotes the quantities before flavor transformation and $P_{\nu_e\to\nu_s}(E) = 1 - P_{\nu_e\to\nu_e}(E)$ and $n^0_{\nu_e}(E, r_i)$ is extracted from our benchmark hydrodynamical simulation. A similar expression holds for $P_{\bar{\nu}_e\to\bar{\nu}_e}$.

Figure 3 shows the survival probability of ν_e's and $\bar{\nu}_e$'s for $(\sin^2\theta_v, \Delta m^2) = (10^{-2}, 10^{-1}\ \mathrm{eV}^2)$ and a selected neutrino energy $E = 20$ MeV, obtained by solving Eqs. (3) and (4) numerically [with initial conditions $n^0_{\nu_e}(E, r_0)$ and

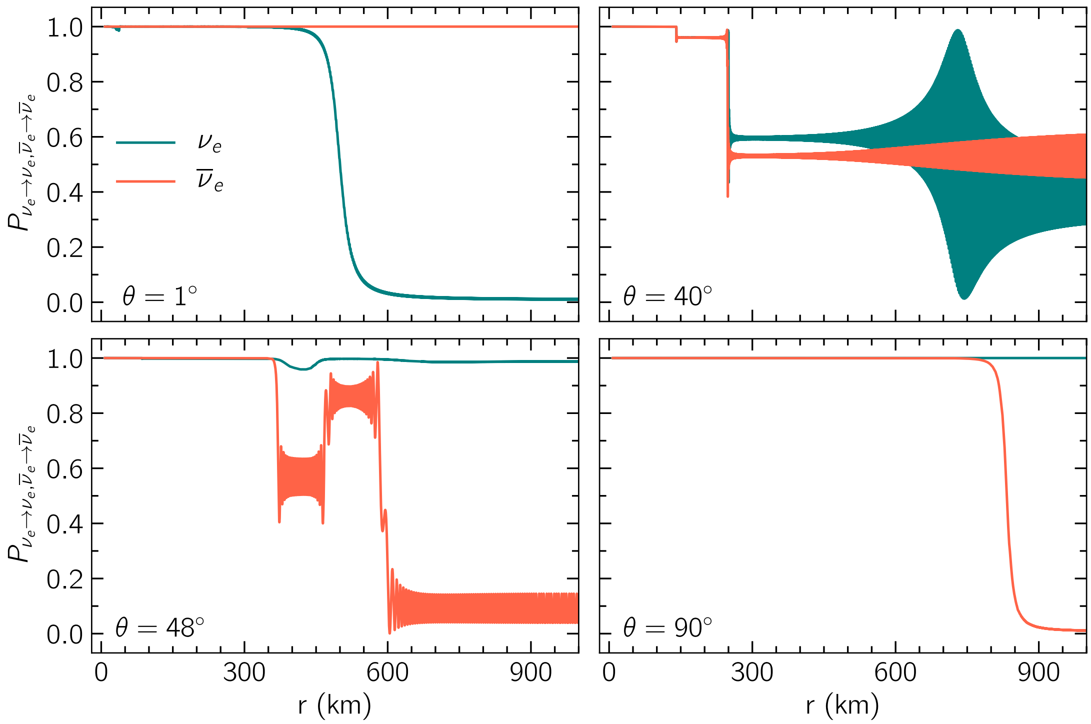

FIG. 3. Survival probabilities for ν_e (in green) and $\bar{\nu}_e$ (in red) with $E = 20$ MeV and $(\sin^2\theta_v, \Delta m^2) = (10^{-2}, 10^{-1}\ \mathrm{eV}^2)$ for $\theta = 1°$, 40°, 48°, and 90° from the top left panel to the bottom right panel, respectively. A varying number of resonances occurs for neutrinos and antineutrinos, depending on θ, as visible from Fig. 2. Moreover, because of the spatial variation of the effective matter potential, the adiabaticity of flavor conversion changes as a function of the radius.

$n^0_{\bar{\nu}_e}(E, r_0)$ extracted from our benchmark merger simulation at the innermost radius r_0] and applying Eq. (13).[2] We warn the reader that the resonance radii in Fig. 3 depend on the neutrino energy and the active-sterile mixing parameters; MSW resonances at smaller radii should be expected for larger Δm^2 (see Sec. IV).

The same computation can be carried out analytically. In this case, the neutrino number density at each resonance radius r_i, occurring after neutrino decoupling, is

$$n_{\nu_e}(E, r_i) = P_{\nu_e\to\nu_e}(E, r_i) n_{\nu_e}(E, r_{i-1}) \left(\frac{r_{i-1}}{r_i}\right)^2 + P_{\nu_s\to\nu_e}(E, r_i) n_{\nu_s}(E, r_{i-1}) \left(\frac{r_{i-1}}{r_i}\right)^2, \quad (14)$$

with the survival probability being computed through Eq. (11) and $i-1$ being the former resonance in the event that multiple resonances take place (see Fig. 2). By comparing with the outputs of our benchmark hydrodynamical simulation, we verified that the neutrino number density at r_{i-1} can be safely rescaled by $\sim 1/r^2$ in order to compute the local number density at r_i. However, a special case occurs for the first resonance, where $n_{\nu_e}(E, r_1) = P_{\nu_e\to\nu_e}(E, r_1) n_{\nu_e}(E, r_1)$, with $n_{\nu_e}(E, r_1)$ being extracted from our benchmark remnant simulation model. Moreover, for $\theta = 90°$, the first MSW resonance occurs before neutrino decoupling; hence, $n_{\nu_e}(E, r_2) = P_{\nu_e\to\nu_e}(E, r_2) n_{\nu_e}(E, r_2) + P_{\nu_s\to\nu_e}(E, r_1) n_{\nu_s}(E, r_1)(r_1/r_2)^2$, where $n_{\nu_e}(E, r_2)$ is extracted from our remnant simulation model. Analogous expressions hold for $n_{\nu_s}(E, r_i)$. We find that our analytical computations are in agreement with the numerical ones (results not shown here).

We can see that the flavor conversion physics is highly dependent on the emission direction and that more than two resonances could occur for some directions, as is noticeable in Fig. 2 (see, e.g., $\theta = 48°$). As expected, according to the emission direction and for our fixed neutrino energy, the adiabaticity of flavor conversion changes. This has the effect that ν_s's are minimally produced in the equatorial plane (see $\theta = 90°$), whereas in the polar region no $\bar{\nu}_s$'s are produced, since no $\bar{\nu}_e$–$\bar{\nu}_s$ resonances can occur (see $\theta = 1°$).

We warn the reader that, while our choice of the representative radial directions aims to highlight the diversity of the active-sterile flavor conversion phenomenology,

[2] For $\theta = 90°$, neutrinos undergo flavor conversion before decoupling; hence, the numerical solution of Eqs. (3) and (4) is approximated, since it does not take into account the repopulation term. However, for the mass-mixing parameters adopted in Fig. 3 there is no production of sterile states in the first resonance (due to the highly nonadiabatic MSW resonance), and therefore the result is independent on the repopulation effects. The second resonance occurs in the free-streaming regime, where Eqs. (3) and (4) hold.

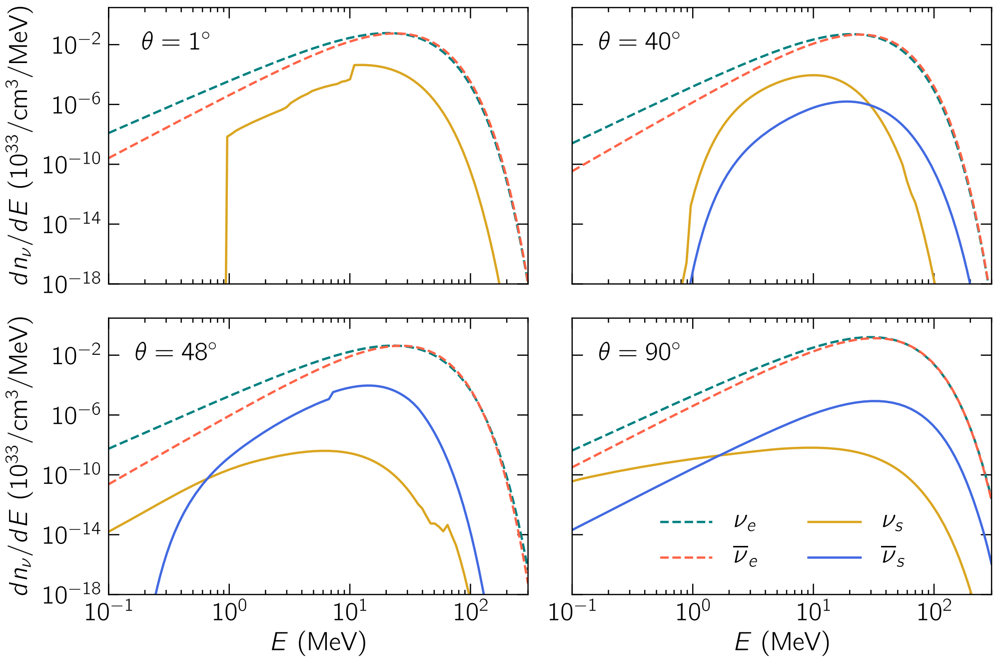

FIG. 4. Differential number densities of ν_e (dashed green line), $\bar{\nu}_e$ (dashed red line), ν_s (solid ochre line), and $\bar{\nu}_s$ (solid blue line) as functions of energy for the same emission directions and mixing parameters as displayed in Fig. 3. The dashed lines have been extracted at the innermost radius 8.02 km and the solid ones at 1000 km. Only sterile neutrinos are produced along $\theta = 1°$, while more sterile antineutrinos than sterile neutrinos are produced along $\theta = 90°$.

not all of our benchmark radial directions have comparable relevance for what concerns the astrophysical implications. In fact, for neutrino paths starting within the neutrino decoupling surfaces, $Y_e \lesssim 1/3$ in the innermost regions; on the other hand, neutrinos start propagating from a region with a high value of λ (i.e., $Y_e \gtrsim 1/3$) toward regions with lower λ ($Y_e \lesssim 1/3$) for $\theta = 40°$ and 48°. As a consequence, for $\theta = 40°$ and 48°, the innermost MSW resonances may appear to be peculiar because the trajectories start on the black-hole horizon (large Y_e). However, we note that neutrinos emitted from the opposite side of the disk and crossing the funnel would have gone through resonances similar to those represented by $\theta = 40°$ and 48°. Thus, our selected radial directions provide a complete picture of the flavor conversion phenomenology.

Interestingly, due to the torus geometry, the flavor conversion phenomenology in NS merger remnants differs from the SN one [73–77], where at most two MSW resonances were observed. However, as in the SN case, the innermost resonances are less adiabatic than the outer ones because of the steep radial profile of λ. Another difference with respect to the SN case is that $\bar{\nu}_e$'s are naturally more abundant in the compact merger scenario.

Figure 4 shows the active and sterile differential number densities as functions of the energy for the same representative mixing parameters and emission directions as shown in Fig. 3. We can see how the effects of the varying adiabaticity and the occurrence of MSW resonances distort the shape of the sterile distributions at 1000 km, creating energy-dependent features. In addition, $\bar{\nu}_s$'s are not produced in the surroundings of the polar region ($\theta = 1°$, top left panel), while more $\bar{\nu}_s$'s than ν_s's are produced near the equatorial region ($\theta = 90°$, bottom right panel).

IV. DEPENDENCE OF THE FLAVOR CONVERSION PHENOMENOLOGY ON THE STERILE MASS AND MIXING PARAMETERS

In this section, we investigate the physics of flavor conversion and the production of sterile particles as functions of the sterile mixing parameters. In what follows, we scan the mass-mixing parameter space considered for light sterile neutrinos [50,52,53]; because of the lack of consensus on the mass-mixing sterile parameters necessary to interpret the various experimental anomalies (see Sec. I), we refrain from choosing benchmark mass-mixing sterile parameters.

A. Occurrence of multiple MSW resonances

In order to compute the average amount of flavor mixing across multiple resonances, we introduce the energy averaged survival probability for neutrinos at each resonance:

$$\langle P_{\nu_e\to\nu_e}(r_i)\rangle = \frac{\int dE P_{\nu_e\to\nu_e}(E, r_i) n_{\nu_e}(E, r_{i-1})}{\int dE n_{\nu_e}(E, r_{i-1})}, \tag{15}$$

with $P_{\nu_e\to\nu_e}(E, r_i)$ defined as in Eq. (11). An analogous expression holds for the survival probability of antineutrinos, $\langle P_{\bar{\nu}_e\to\bar{\nu}_e}(r_i)\rangle$.

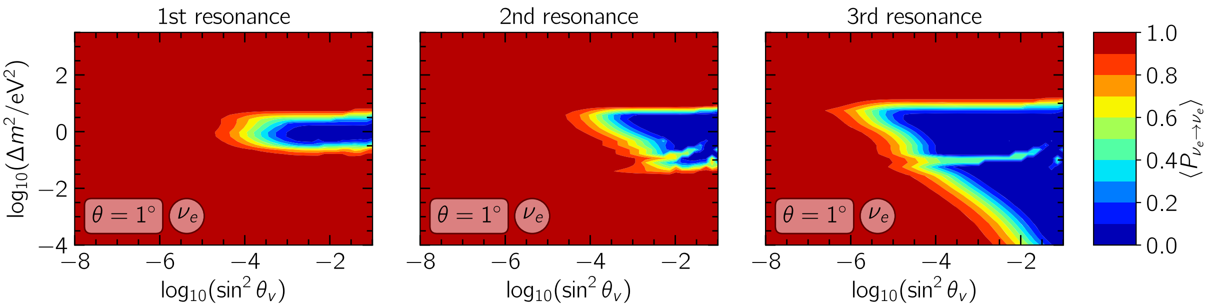

FIG. 5. Contour plot of the ν_e energy averaged survival probability at the three resonances [see Fig. 1 and Eq. (15)] for the emission direction $\theta = 1^\circ$ in the plane spanned by $\sin^2\theta_v$ and Δm^2. Only neutrinos undergo resonances; no MSW resonance occurs for antineutrinos. At the third resonance, the range and slope of the potential (see Fig. 2) allows for a larger region of the mass-mixing parameter space to be affected by full flavor conversion.

Figures 5–8 show contour plots of $\langle P_{\nu_e\to\nu_e}(r_i)\rangle$ ($\langle P_{\bar{\nu}_e\to\bar{\nu}_e}(r_i)\rangle$) in the plane spanned by $(\sin^2\theta_v, \Delta m^2)$ on top (bottom). Each resonance is identified through the number of times $d\lambda/dr$ changes sign, as shown in Fig. 2. The amount of flavor transformation that occurs within each resonance region depends on λ, which controls which $(\sin^2\theta_v, \Delta m^2)$ undergo MSW resonances. On the other hand, $d\lambda/dr$ controls the adiabaticity of each resonance.

There are general features which most resonance regions display, regardless of θ. The region of partial or full flavor

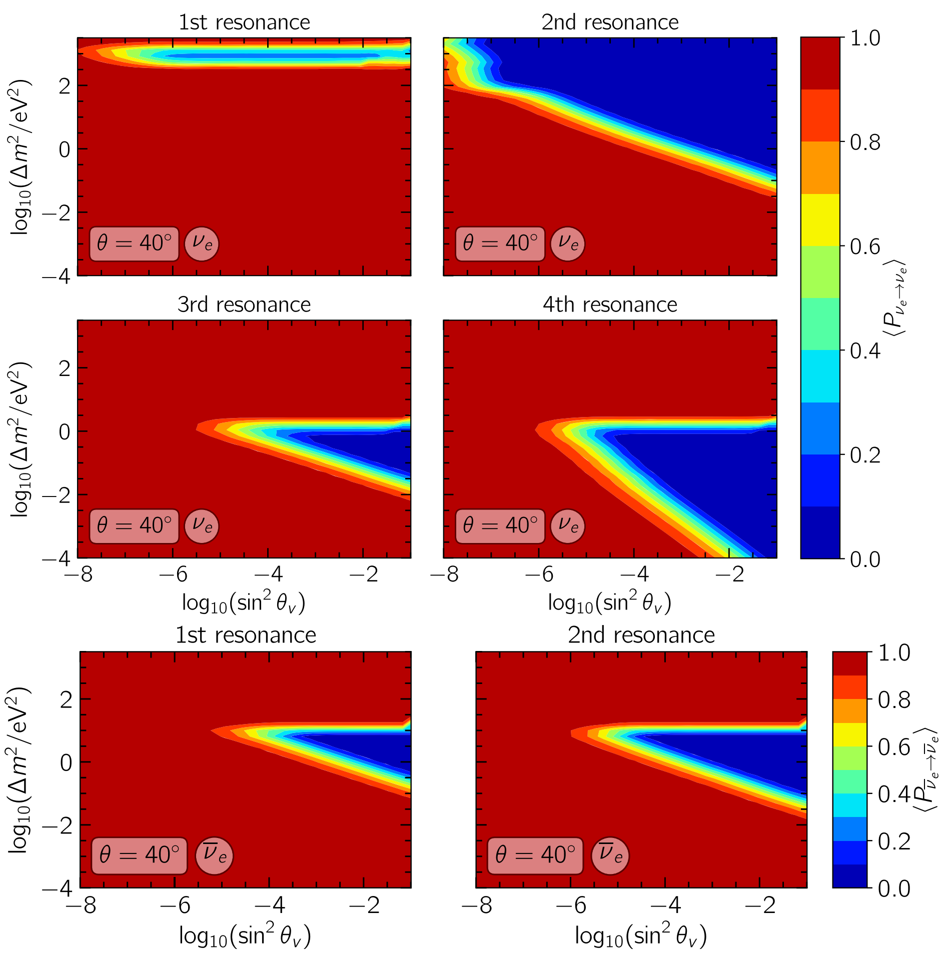

FIG. 6. Same as Fig. 5, but for $\theta = 40^\circ$. Four MSW resonances occur for neutrinos (top panels), and two for antineutrinos (bottom panels). Unlike Fig. 5, the region of the parameter space affected by flavor conversion is not always larger as outer resonances are met (and the matter potential becomes shallower).

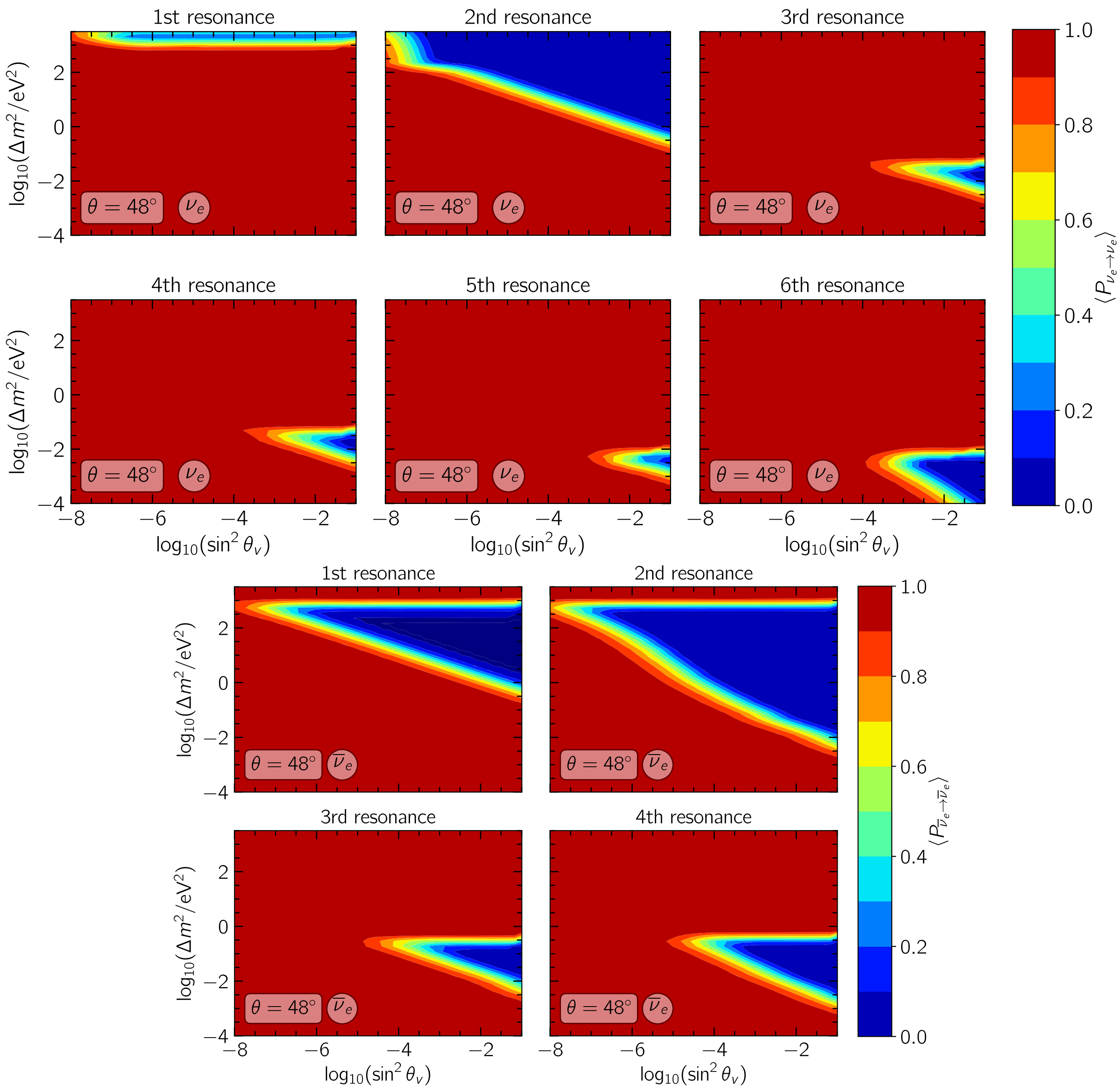

FIG. 7. Same as Fig. 5, but for $\theta = 48°$. Six MSW resonances occur for neutrinos and four for antineutrinos.

conversion into sterile states has a triangular shape. This is because the adidabaticity of the MSW resonance increases as $\sin^2\theta_v$ and/or Δm^2 increase [see Eq. (10)]. These triangular regions are bounded from above in most cases since a high Δm^2 causes $\lambda_{\rm res}$ to exceed the maximum value of the potential λ within that region (or minimum value for antineutrinos), resulting in an absence of resonances for the upper part of the parameter space.

The bottom panels of Fig. 8 represent the survival probability of antineutrinos for $\theta = 90°$. We see how the first resonance is much less adiabatic than the second one. This is due to how rapidly Y_e crosses $1/3$, while ρ_B is still very large, causing $d\lambda/dr \gg 1$; i.e., λ is very steep as it changes sign for the first time (see Fig. 2). A similar trend can be seen in the bottom panels of Figs. 6 and 7 for $\theta = 40$ and 48°, though not as prominently. Otherwise, the same general features in the neutrino survival probability also present themselves in the antineutrino plots.

B. Overall production of sterile neutrinos and antineutrinos

Figures 9 and 10 show the overall number densities of sterile neutrinos and antineutrinos at $r = 1000$ km, respectively, produced through multiple MSW resonances. The lowest number density of resonantly produced sterile particles is visible in the bottom left corner of the $(\sin^2\theta_v, \Delta m^2)$ plane for all panels of Figs. 9 and 10. In general, as $\sin^2\theta_v$ increases, the number density of sterile neutrinos in Fig. 9 increases. The shape of the contours closely follows the patterns shown in Figs. 5–8 and is a direct consequence of multiple resonances. As expected,

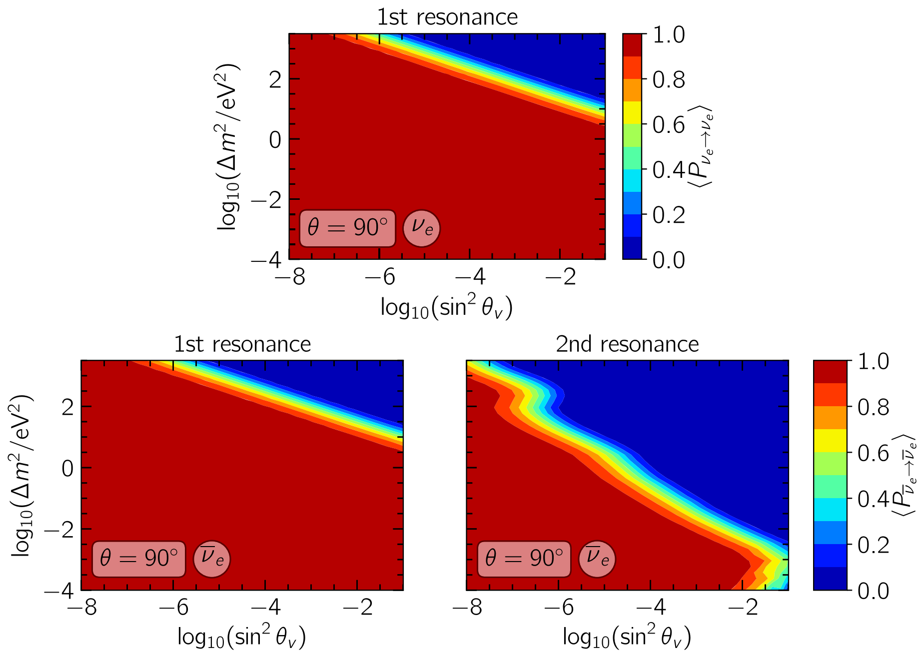

FIG. 8. Same as Fig. 5, but for $\theta = 90°$. One MSW resonance takes place for neutrinos and two for antineutrinos.

sterile neutrinos are abundantly produced for a larger region of the mass-mixing parameter space for $\theta = 1°$.

In the top panels of Fig. 10 (for $\theta = 40°, 48°$), the combined effect of all MSW resonances can be observed in the asymptotic emission of $\bar{\nu}_s$'s. On the other hand, in the bottom panel of Fig. 10 ($\theta = 90°$), the effect of the first resonance is not visible in the top right part of the parameter space. This is because $\bar{\nu}_s$'s generated adiabatically at the

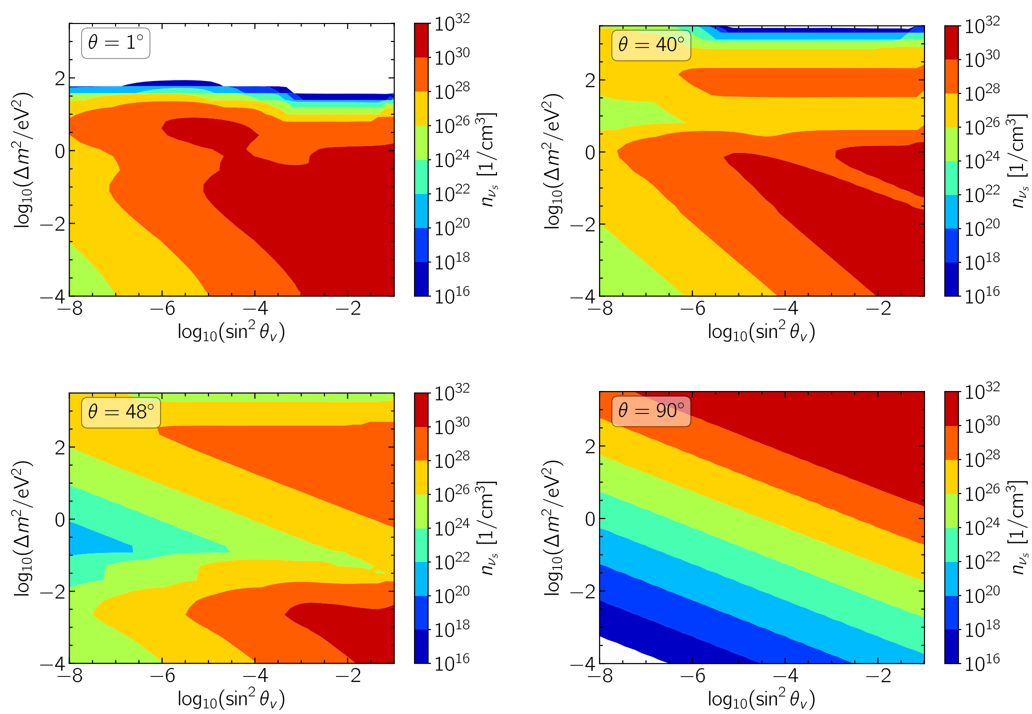

FIG. 9. Contour plot of the number density of sterile neutrinos at 1000 km in the plane spanned by $(\sin^2\theta_V, \Delta m^2)$ for $\theta = 1°, 40°, 48°$, and 90° from top left to bottom right, respectively. The number density of sterile neutrinos is maximal for a large region of the mass-mixing parameter space for $\theta = 1°$.

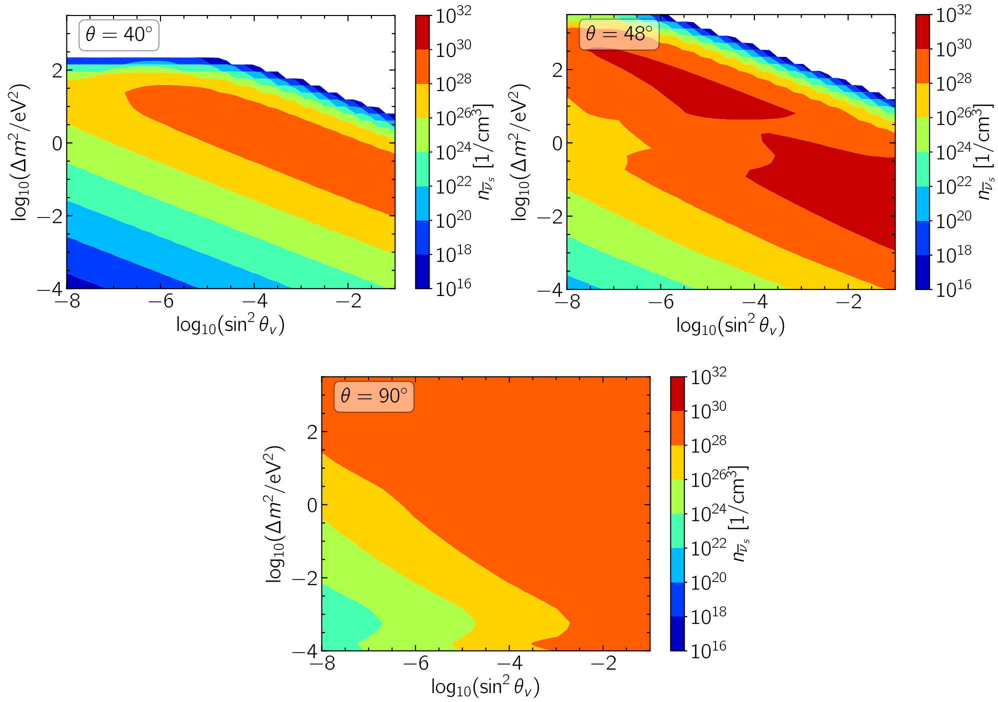

FIG. 10. Same as Fig. 9, but for sterile antineutrinos. The contour plot for $\theta = 1°$ is omitted as no production of $\bar{\nu}_s$'s occurs. The number density of sterile antineutrinos is maximal for a large region of the mass-mixing parameter space for $\theta = 90°$.

first resonance are reconverted back to $\bar{\nu}_e$'s at the second resonance. Thus, $n_{\bar{\nu}_s}$ in our plot is determined by the conversions into sterile states occurring at the second resonance; on the other hand, flavor conversion at the first and second resonances leads to an enhanced $n_{\bar{\nu}_e}$ in the top right corner of the parameter space.

V. ACTIVE-STERILE FLAVOR CONVERSION AS A FUNCTION OF THE TORUS EVOLUTION

In this section, we explore the active-sterile flavor conversion physics for three snapshots of the disk evolution ($t = 10$, 25, and 50 ms) and a fixed emission angle $\theta = 90°$. The matter potential λ is shown in Fig. 11. One can see that

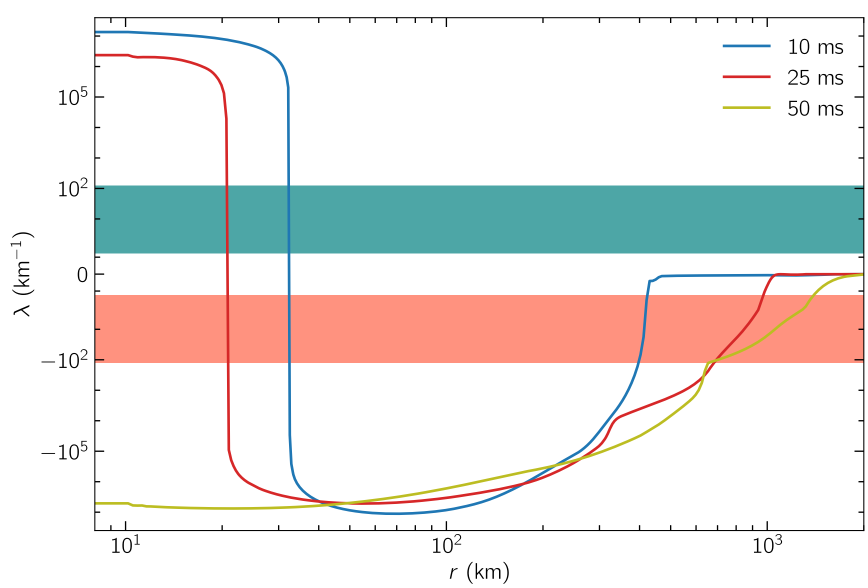

FIG. 11. Effective matter potential λ as a function of the radius for three different time snapshots, $t = 10$, 25, and 50 ms in the equatorial plane, i.e., for $\theta = 90°$. The green and red bands show λ_{res} for $(\sin^2\theta_v, \Delta m^2) = (10^{-2}, 10^{-1}\ \mathrm{eV}^2)$ and $E \in [0.1, 300]$ MeV for neutrinos and antineutrinos, respectively. As λ evolves as a function of time, the number of MSW resonances changes.

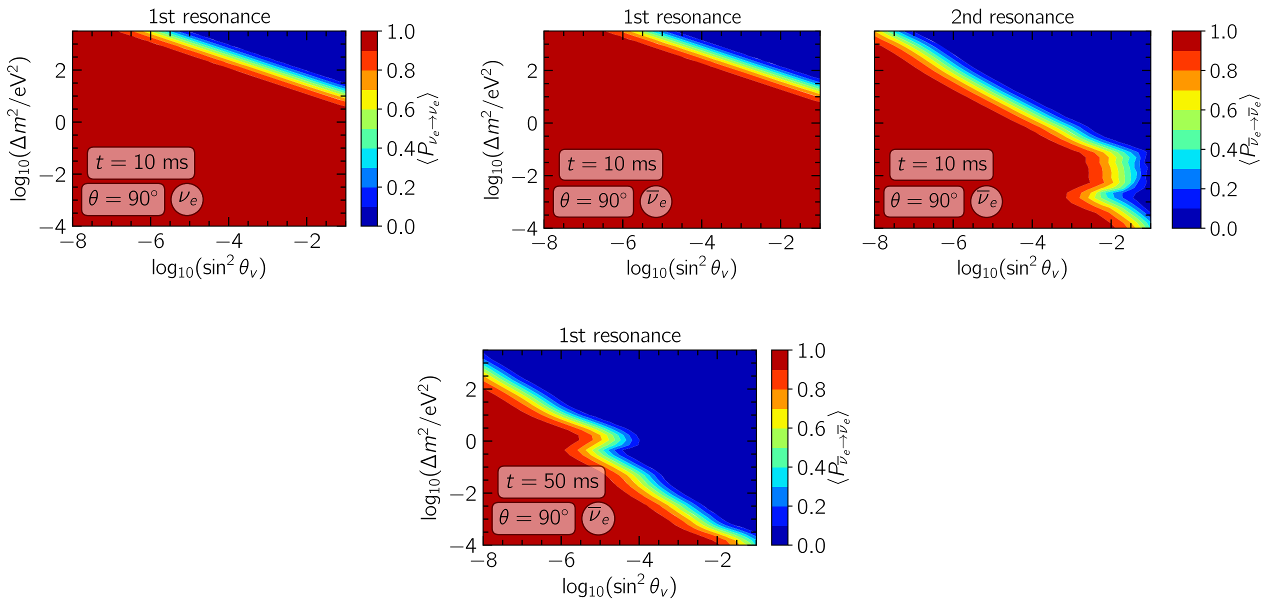

FIG. 12. Contour plot of the ν_e and $\bar{\nu}_e$ energy averaged survival probabilities for the emission direction $\theta = 90°$ at $t = 10$ ms (top panels, for ν_e's and $\bar{\nu}_e$'s) and 50 ms (bottom panel, for $\bar{\nu}_e$'s). As time increases, the region of the mass-mixing parameter space affected by flavor conversion becomes larger.

the MSW resonance patterns are similar to the ones investigated in Fig. 2 for $t = 25$ ms. Features similar to those illustrated in Fig. 2 can be found for the radial profiles of λ along the polar region and for some intermediate values of θ. However, in the proximity of the equatorial plane ($\theta = 90°$), the electron fraction drops, causing λ to change sign in the innermost regions for $t > 25$ ms. As a consequence, no MSW resonances occur for ν_e at $t = 50$ ms, and one fewer MSW resonance takes place for $\bar{\nu}_e$ with respect to the $t = 25$ ms case. Nevertheless, since the innermost resonances were mainly nonadiabatic, we do not find large changes in the overall flavor conversion physics, as shown in Fig. 12 (see Fig. 8 for comparison).

As t increases, the matter gradient along the radial directions becomes gentler because of the drop in baryon density, resulting in more adiabatic resonances and a larger region of the mass-mixing parameter space affected by flavor conversion at $t = 50$ ms than at $t = 10$ ms, as can be seen in Fig. 12.

VI. OUTLOOK

By relying on a two-flavor framework (one active plus one sterile species), we have explored the active-sterile flavor conversion phenomenology in compact binary merger remnants for the first time. We have investigated the production of sterile states as a function of the sterile neutrino mixing parameters, representative radial directions of neutrino emission from the accretion torus, and temporal evolution of the merger remnant.

Because of the torus geometry and the neutron richness of the environment, large flavor conversion occurs for antineutrinos. In particular, unlike the SN case, we find that multiple (up to six; see Fig. 2) MSW resonances can take place, depending upon the neutrino emission direction. It is important to stress that, while our representative radial directions highlight differences in the active-sterile flavor conversion phenomenology, the impact of active-sterile neutrino conversion on the physics of the remnant is direction dependent. However, an assessment of the latter is beyond the scope of this work. The torus geometry is responsible for a large production of sterile neutrinos (and no antineutrinos) near the polar region, and more sterile antineutrinos than neutrinos in the equatorial region. While we rely on the output of one hydrodynamical simulation of a BH accretion torus [23], our main conclusions should be generic, as they are fundamentally linked to the characteristic properties and geometry of binary merger remnants.

As the BH torus evolves, the active-sterile oscillation phenomenology remains unchanged overall. However, the shallower baryon density at later times is responsible for more adiabatic flavor conversion that leads to a larger region of the mass-mixing parameter space being affected by active-sterile flavor conversion.

Our findings rely on a simplified framework for what concerns the modeling of the flavor conversion physics. We neglect any impact of neutrino-neutrino interaction on the active-sterile neutrino conversion because of the uncertainties currently involved in our understanding of this phenomenon and the related numerical challenges. Yet, within a simplified framework, it has been proven that neutrino self-interaction could further affect the active-sterile conversion physics in the SN context [74–77].

Despite the caveats of our modeling, our results robustly suggest that the nontrivial active-sterile flavor phenomenology occurring in merger remnants can have indirect implications on the disk cooling rate and its outflows. For instance, by relying on the findings of Ref. [40], we deduce that the adiabaticity of ν_e and $\bar{\nu}_e$ flavor conversion into sterile states inside the neutrino sphere (see, e.g., the first resonance panel of Fig. 8 for $\theta = 90°$) could potentially accelerate the cooling of the remnant disk and lower Y_e in the disk in a fashion similar to what was discussed in Ref. [40]. In addition, flavor conversion occurring in the polar region at radii of $\mathcal{O}(100)$ km (see, e.g., Figs. 2 or 3) would also reduce the neutrino capture rates by nucleons in the polar outflows, where Y_e and the nucleosynthesis outcomes are sensitive to the abundance of the electron flavors, as in the scenario considered in Ref. [38].

A robust assessment of the impact of the active-sterile flavor conversion physics on the electromagnetic observables as well as on the disk cooling rate are left to future work, to be conducted after a reliable modeling of the active-active conversion physics in the presence of neutrino self-interactions becomes available. In order to place robust constraints on the sterile mixing parameters through future multimessenger observations, a survey of the flavor conversion phenomenology for various compact binary merger models and related feedback on the observables will be required. This work proves the unexplored potential of upcoming multimessenger observations of compact binary merger remnants to unveil the existence of sterile neutrinos.

ACKNOWLEDGMENTS

We would like to thank Oliver Just for the insightful discussions. We acknowledge support from the Villum Foundation (Project No. 13164), the Carlsberg Foundation (Grant No. CF18-0183), the Deutsche Forschungsgemeinschaft through Sonderforschungbereich SFB 1258 "Neutrinos and Dark Matter in Astro- and Particle Physics" (NDM), the National Science and Technology Council, Taiwan, under Grants No. 110-2112-M-001-050 and No. 111-2628-M-001-003-MY4, the Academia Sinica (Project No. AS-CDA-109-M11), and the Physics Division of the National Center for Theoretical Sciences, Taiwan.

[1] Raffaella Margutti and Ryan Chornock, First multimessenger observations of a neutron star merger, Annu. Rev. Astron. Astrophys. **59**, 155 (2021).

[2] Benjamin P. Abbott *et al.* (LIGO Scientific and Virgo Collaborations), GW170817: Observation of Gravitational Waves from a Binary Neutron Star Inspiral, Phys. Rev. Lett. **119**, 161101 (2017).

[3] Benjamin P. Abbott *et al.* (LIGO Scientific, Virgo, Fermi-GBM, and INTEGRAL Collaborations), Gravitational waves and gamma-rays from a binary neutron star merger: GW170817 and GRB 170817A, Astrophys. J. Lett. **848**, L13 (2017).

[4] Benjamin P. Abbott *et al.* (LIGO Scientific, Virgo, Fermi GBM, INTEGRAL, IceCube, AstroSat Cadmium Zinc Telluride Imager Team, IPN, Insight-Hxmt, ANTARES, Swift, AGILE Team, 1M2H Team, Dark Energy Camera GW-EM, DES, DLT40, GRAWITA, Fermi-LAT, ATCA, ASKAP, Las Cumbres Observatory Group, OzGrav, DWF (Deeper Wider Faster Program), AST3, CAASTRO, VINROUGE, MASTER, J-GEM, GROWTH, JAGWAR, CaltechNRAO, TTU-NRAO, NuSTAR, Pan-STARRS, MAXI Team, TZAC Consortium, KU, Nordic Optical Telescope, ePESSTO, GROND, Texas Tech University, SALT Group, TOROS, BOOTES, MWA, CALET, IKI-GW Follow-up, H.E.S.S., LOFAR, LWA, HAWC, Pierre Auger, ALMA, Euro VLBI Team, Pi of Sky, Chandra Team at McGill University, DFN, ATLAS Telescopes, High Time Resolution Universe Survey, RIMAS, RATIR, and SKA South Africa/MeerKAT Collaborations), Multi-messenger observations of a binary neutron star merger, Astrophys. J. Lett. **848**, L12 (2017).

[5] Adam Goldstein *et al.*, An ordinary short gamma-ray burst with extraordinary implications: Fermi-GBM detection of GRB 170817A, Astrophys. J. Lett. **848**, L14 (2017).

[6] Volodymyr Savchenko *et al.*, INTEGRAL detection of the first prompt gamma-ray signal coincident with the gravitational-wave event GW170817, Astrophys. J. Lett. **848**, L15 (2017).

[7] Raffaella Margutti *et al.*, The electromagnetic counterpart of the binary neutron star merger LIGO/VIRGO GW170817. V. Rising x-ray emission from an off-axis jet, Astrophys. J. Lett. **848**, L20 (2017).

[8] Eleonora Troja *et al.*, The x-ray counterpart to the gravitational wave event GW 170817, Nature (London) **551**, 71 (2017).

[9] Daniel Kasen, Brian Metzger, Jennifer Barnes, Eliot Quataert, and Enrico Ramirez-Ruiz, Origin of the heavy elements in binary neutron-star mergers from a gravitational wave event, Nature (London) **551**, 80 (2017).

[10] Maria R. Drout *et al.*, Light curves of the neutron star merger GW170817/SSS17a: Implications for r-process nucleosynthesis, Science **358**, 1570 (2017).

[11] Philip S. Cowperthwaite *et al.*, The electromagnetic counterpart of the binary neutron star merger LIGO/Virgo GW170817. II. UV, optical, and near-infrared light curves and comparison to kilonova models, Astrophys. J. Lett. **848**, L17 (2017).

[12] V. Ashley Villar *et al.*, The combined ultraviolet, optical, and near-infrared light curves of the kilonova associated

with the binary neutron star merger GW170817: Unified data set, analytic models, and physical implications, Astrophys. J. Lett. **851**, L21 (2017).

[13] Masaru Shibata, Sho Fujibayashi, Kenta Hotokezaka, Kenta Kiuchi, Koutarou Kyutoku, Yuichiro Sekiguchi, and Masaomi Tanaka, Modeling GW170817 based on numerical relativity and its implications, Phys. Rev. D **96**, 123012 (2017).

[14] Brian D. Metzger, Kilonovae, Living Rev. Relativity **23**, 1 (2020).

[15] Doğa Veske, Zsuzsa Márka, Imre Bartos, and Szabolcs Márka, Neutrino emission upper limits with maximum likelihood estimators for joint astrophysical neutrino searches with large sky localizations, J. Cosmol. Astropart. Phys. 05 (2020) 016.

[16] Mark G. Aartsen *et al.* (IceCube Collaboration), IceCube search for neutrinos coincident with compact binary mergers from LIGO-Virgo's first gravitational-wave transient catalog, Astrophys. J. Lett. **898**, L10 (2020).

[17] Yoshinari Hayato *et al.* (Super-Kamiokande Collaboration), Search for neutrinos in Super-Kamiokande associated with the GW170817 neutron-star merger, Astrophys. J. Lett. **857**, L4 (2018).

[18] Francois Foucart, Evan O'Connor, Luke Roberts, Matthew D. Duez, Roland Haas, Lawrence E. Kidder, Christian D. Ott, Harald P. Pfeiffer, Mark A. Scheel, and Bela Szilagyi, Post-merger evolution of a neutron star-black hole binary with neutrino transport, Phys. Rev. D **91**, 124021 (2015).

[19] Maximilian Ruffert, H.-Thomas Janka, Kazuya Takahashi, and Gerhard Schaefer, Coalescing neutron stars: A step towards physical models. II. Neutrino emission, neutron tori, and gamma-ray bursts, Astron. Astrophys. **319**, 122 (1997), https://ui.adsabs.harvard.edu/abs/1997A%26A...319..122R/abstract.

[20] Brian D. Metzger and Rodrigo Fernández, Red or blue? A potential kilonova imprint of the delay until black hole formation following a neutron star merger, Mon. Not. R. Astron. Soc. **441**, 3444 (2014).

[21] Albino Perego, Stephan Rosswog, Ruben M. Cabezón, Oleg Korobkin, Roger Käppeli, Almudena Arcones, and Matthias Liebendörfer, Neutrino-driven winds from neutron star merger remnants, Mon. Not. R. Astron. Soc. **443**, 3134 (2014).

[22] Shinya Wanajo, Yuichiro Sekiguchi, Nobuya Nishimura, Kenta Kiuchi, Koutarou Kyutoku, and Masaru Shibata, Production of all the *r*-process nuclides in the dynamical ejecta of neutron star mergers, Astrophys. J. Lett. **789**, L39 (2014).

[23] Oliver Just, Andreas Bauswein, Ricard Ardevol Pulpillo, Stephane Goriely, and H.-Thomas Janka, Comprehensive nucleosynthesis analysis for ejecta of compact binary mergers, Mon. Not. R. Astron. Soc. **448**, 541 (2015).

[24] Sho Fujibayashi, Masaru Shibata, Shinya Wanajo, Kenta Kiuchi, Koutarou Kyutoku, and Yuichiro Sekiguchi, Mass ejection from disks surrounding a low-mass black hole: Viscous neutrino-radiation hydrodynamics simulation in full general relativity, Phys. Rev. D **101**, 083029 (2020).

[25] Ina Kullmann, Stephan Goriely, Oliver Just, Ricard Ardevol-Pulpillo, Andreas Bauswein, and H.-Thomas Janka, Dynamical ejecta of neutron star mergers with nucleonic weak processes I: Nucleosynthesis, Mon. Not. R. Astron. Soc. **510**, 2804 (2022).

[26] Ramesh Narayan, Bohdan Paczynski, and Tsvi Piran, Gamma-ray bursts as the death throes of massive binary stars, Astrophys. J. Lett. **395**, L83 (1992).

[27] Edo Berger, Short-duration gamma-ray bursts, Annu. Rev. Astron. Astrophys. **52**, 43 (2014).

[28] Oliver Just, Martin Obergaulinger, H.-Thomas Janka, Andreas Bauswein, and Nicole Schwarz, Neutron-star merger ejecta as obstacles to neutrino-powered jets of gamma-ray bursts, Astrophys. J. Lett. **816**, L30 (2016).

[29] Annelise Malkus, Alexander Friedland, and Gail C. McLaughlin, Matter-neutrino resonance above merging compact objects, arXiv:1403.5797.

[30] Annelise Malkus, James P. Kneller, Gail C. McLaughlin, and Rebecca Surman, Neutrino oscillations above black hole accretion disks: Disks with electron-flavor emission, Phys. Rev. D **86**, 085015 (2012).

[31] Meng-Ru Wu, Huaiyu Duan, and Yong-Zhong Qian, Physics of neutrino flavor transformation through matter–neutrino resonances, Phys. Lett. B **752**, 89 (2016).

[32] Yong-Lin Zhu, Albino Perego, and Gail C. McLaughlin, Matter neutrino resonance transitions above a neutron star merger remnant, Phys. Rev. D **94**, 105006 (2016).

[33] Maik Frensel, Meng-Ru Wu, Cristina Volpe, and Albino Perego, Neutrino flavor evolution in binary neutron star merger remnants, Phys. Rev. D **95**, 023011 (2017).

[34] James Y. Tian, Amol V. Patwardhan, and George M. Fuller, Neutrino flavor evolution in neutron star mergers, Phys. Rev. D **96**, 043001 (2017).

[35] Shashank Shalgar, Multi-angle calculation of the matter-neutrino resonance near an accretion disk, J. Cosmol. Astropart. Phys. 02 (2018) 010.

[36] Irene Tamborra and Shashank Shalgar, New developments in flavor evolution of a dense neutrino gas, Annu. Rev. Nucl. Part. Sci. **71**, 165 (2021).

[37] Meng-Ru Wu and Irene Tamborra, Fast neutrino conversions: Ubiquitous in compact binary merger remnants, Phys. Rev. D **95**, 103007 (2017).

[38] Meng-Ru Wu, Irene Tamborra, Oliver Just, and H.-Thomas Janka, Imprints of neutrino-pair flavor conversions on nucleosynthesis in ejecta from neutron-star merger remnants, Phys. Rev. D **96**, 123015 (2017).

[39] Manu George, Meng-Ru Wu, Irene Tamborra, Ricard Ardevol-Pulpillo, and H.-Thomas Janka, Fast neutrino flavor conversion, ejecta properties, and nucleosynthesis in newly-formed hypermassive remnants of neutron-star mergers, Phys. Rev. D **102**, 103015 (2020).

[40] Oliver Just, Sajad Abbar, Meng-Ru Wu, Irene Tamborra, H.-Thomas Janka, and Francesco Capozzi, Fast neutrino conversion in hydrodynamic simulations of neutrino-cooled accretion disks, Phys. Rev. D **105**, 083024 (2022).

[41] Xinyu Li and Daniel M. Siegel, Neutrino Fast Flavor Conversions in Neutron-Star Postmerger Accretion Disks, Phys. Rev. Lett. **126**, 251101 (2021).

[42] Rodrigo Fernández, Sherwood Richers, Nicole Mulyk, and Steven Fahlman, The fast flavor instability in hypermassive neutron star disk outflows, Phys. Rev. D **106**, 103003 (2022).

[43] Rafael Alves Batista *et al.*, EuCAPT white paper: Opportunities and challenges for theoretical astroparticle physics in the next decade, arXiv:2110.10074.

[44] Eric Burns, Neutron star mergers and how to study them, Living Rev. Relativity **23**, 4 (2020).

[45] Eric Burns *et al.*, A summary of multimessenger science with neutron star mergers, arXiv:1903.03582.

[46] Nancy Aggarwal *et al.*, Challenges and opportunities of gravitational-wave searches at MHz to GHz frequencies, Living Rev. Relativity **24**, 4 (2021).

[47] Melissa D. Diamond and Gustavo Marques-Tavares, γ-Ray Flashes from Dark Photons in Neutron Star Mergers, Phys. Rev. Lett. **128**, 211101 (2022).

[48] Zurab Berezhiani and Alessandro Drago, Gamma-ray bursts via emission of axion-like particles, Phys. Lett. B **473**, 281 (2000).

[49] Zurab Berezhiani, Ignazio Bombaci, Alessandro Drago, Filippo Frontera, and Andrea Lavagno, Gamma-ray bursts from delayed collapse of neutron stars to quark matter stars, Astrophys. J. **586**, 1250 (2003).

[50] Basudeb Dasgupta and Joachim Kopp, Sterile neutrinos, Phys. Rep. **928**, 1 (2021).

[51] Kevork N. Abazajian *et al.*, Light sterile neutrinos: A white paper, arXiv:1204.5379.

[52] Sebastian Böser, Christian Buck, Carlo Giunti, Julien Lesgourgues, Livia Ludhova, Susanne Mertens, Anne Schukraft, and Michael Wurm, Status of light sterile neutrino searches, Prog. Part. Nucl. Phys. **111**, 103736 (2020).

[53] Mario A. Acero *et al.*, White paper on light sterile neutrino searches and related phenomenology, arXiv:2203.07323.

[54] Alexis A. Aguilar-Arevalo *et al.* (LSND Collaboration), Evidence for neutrino oscillations from the observation of $\bar{\nu}_e$ appearance in a $\bar{\nu}_\mu$ beam, Phys. Rev. D **64**, 112007 (2001).

[55] Alexis A. Aguilar-Arevalo *et al.* (MiniBooNE Collaboration), Updated MiniBooNE neutrino oscillation results with increased data and new background studies, Phys. Rev. D **103**, 052002 (2021).

[56] Thomas A. Mueller *et al.*, Improved predictions of reactor antineutrino spectra, Phys. Rev. C **83**, 054615 (2011).

[57] Patrick Huber, On the determination of anti-neutrino spectra from nuclear reactors, Phys. Rev. C **84**, 024617 (2011); Erratum, Phys. Rev. C **85**, 029901 (2012).

[58] Carlo Giunti, Yufeng Li, Christoph A. Ternes, and Zhao Xin, Reactor antineutrino anomaly in light of recent flux model refinements, Phys. Lett. B **829**, 137054 (2022).

[59] V. Kopeikin, M. Skorokhvatov, and O. Titov, Reevaluating reactor antineutrino spectra with new measurements of the ratio between U235 and Pu239 β spectra, Phys. Rev. D **104**, L071301 (2021).

[60] Jeffrey M. Berryman and Patrick Huber, Sterile neutrinos and the global reactor antineutrino dataset, J. High Energy Phys. 01 (2021) 167.

[61] Manoa Andriamirado *et al.* (PROSPECT and STEREO Collaborations), Note on arXiv:2005.05301, "Preparation of the Neutrino-4 experiment on search for sterile neutrino and the obtained results of measurements", arXiv:2006.13147

[62] Jeffrey M. Berryman, Pilar Coloma, Patrick Huber, Thomas Schwetz, and Albert Zhou, Statistical significance of the sterile-neutrino hypothesis in the context of reactor and gallium data, J. High Energy Phys. 02 (2022) 055.

[63] Carlo Giunti and Marco Laveder, Statistical significance of the gallium anomaly, Phys. Rev. C **83**, 065504 (2011).

[64] Vladislav V. Barinov *et al.*, Results from the Baksan Experiment on Sterile Transitions (BEST). Phys. Rev. Lett. **128**, 232501 (2022).

[65] Vladislav V. Barinov and Dmitry Gorbunov, BEST impact on sterile neutrino hypothesis, Phys. Rev. D **105**, L051703 (2022).

[66] Mona Dentler, Álvaro Hernández-Cabezudo, Joachim Kopp, Pedro A. N. Machado, Michele Maltoni, Ivan Martinez-Soler, and Thomas Schwetz, Updated global analysis of neutrino oscillations in the presence of eV-scale sterile neutrinos, J. High Energy Phys. 08 (2018) 010.

[67] Carlos A. Argüelles, Ivan Esteban, Matheus Hostert, Kevin J. Kelly, Joachim Kopp, Pedro A. N. Machado, Ivan Martinez-Soler, and Yuber F. Perez-Gonzalez, MicroBooNE and the νe Interpretation of the MiniBooNE Low-Energy Excess, Phys. Rev. Lett. **128**, 241802 (2022).

[68] C. Giunti, Y. F. Li, C. A. Ternes, O. Tyagi, and Z. Xin, Gallium anomaly: Critical view from the global picture of ν_e and $\bar{\nu}_e$ disappearance, J. High Energy Phys. 10 (2022) 164.

[69] Steffen Hagstotz, Pablo F. de Salas, Stefano Gariazzo, Martina Gerbino, Massimiliano Lattanzi, Sunny Vagnozzi, Katherine Freese, and Sergio Pastor, Bounds on light sterile neutrino mass and mixing from cosmology and laboratory searches, Phys. Rev. D **104**, 123524 (2021).

[70] Steen Hannestad, Irene Tamborra, and Thomas Tram, Thermalisation of light sterile neutrinos in the early Universe, J. Cosmol. Astropart. Phys. 07 (2012) 025.

[71] Xiaoyong Chu, Basudeb Dasgupta, Mona Dentler, Joachim Kopp, and Ninetta Saviano, Sterile neutrinos with secret interactions—Cosmological discord?, J. Cosmol. Astropart. Phys. 11 (2018) 049.

[72] Maria Archidiacono, Stefano Gariazzo, Carlo Giunti, Steen Hannestad, and Thomas Tram, Sterile neutrino self-interactions: H_0 tension and short-baseline anomalies, J. Cosmol. Astropart. Phys. 12 (2020) 029.

[73] Hiroshi Nunokawa, Juha T. Peltoniemi, Anna Rossi, and Jose W. F. Valle, Supernova bounds on resonant active sterile neutrino conversions, Phys. Rev. D **56**, 1704 (1997).

[74] Irene Tamborra, Georg G. Raffelt, Lorenz Hüdepohl, and H.-Thomas Janka, Impact of eV-mass sterile neutrinos on neutrino-driven supernova outflows, J. Cosmol. Astropart. Phys. 01 (2012) 013.

[75] Meng-Ru Wu, Tobias Fischer, Lutz Huther, Gabriel Martínez-Pinedo, and Yong-Zhong Qian, Impact of active-sterile neutrino mixing on supernova explosion and nucleosynthesis, Phys. Rev. D **89**, 061303 (2014).

[76] Else Pllumbi, Irene Tamborra, Shinya Wanajo, H.-Thomas Janka, and Lorenz Hüdepohl, Impact of neutrino flavor oscillations on the neutrino-driven wind nucleosynthesis of an electron-capture supernova, Astrophys. J. **808**, 188 (2015).

[77] Zewei Xiong, Meng-Ru Wu, and Yong-Zhong Qian, Active-sterile neutrino oscillations in neutrino-driven winds: Implications for nucleosynthesis, Astrophys. J. **880**, 81 (2019).

[78] Arman Esmaili, Orlando L. G. Peres, and Pasquale Dario Serpico, Impact of sterile neutrinos on the early time flux from a galactic supernova, Phys. Rev. D **90**, 033013 (2014).
[79] Jian Tang, Tsechun Wang, and Meng-Ru Wu, Constraining sterile neutrinos by core-collapse supernovae with multiple detectors, J. Cosmol. Astropart. Phys. 10 (2020) 038.
[80] Tina Leitner, Luis Alvarez-Ruso, and Ulrich Mosel, Neutral current neutrino-nucleus interactions at intermediate energies, Phys. Rev. C **74**, 065502 (2006).
[81] Steen Hannestad and Georg G. Raffelt, Supernova neutrino opacity from nucleon-nucleon bremsstrahlung and related processes, Astrophys. J. **507**, 339 (1998).
[82] Alessandro Strumia and Francesco Vissani, Precise quasielastic neutrino/nucleon cross-section, Phys. Lett. B **564**, 42 (2003).
[83] Giulia Ricciardi, Natascia Vignaroli, and Francesco Vissani, An accurate evaluation of electron (anti-)neutrino scattering on nucleons, J. High Energy Phys. 08 (2022) 212.
[84] Anna M. Suliga, Irene Tamborra, and Meng-Ru Wu, Lifting the core-collapse supernova bounds on keV-mass sterile neutrinos, J. Cosmol. Astropart. Phys. 08 (2020) 018.
[85] Anna M. Suliga, Irene Tamborra, and Meng-Ru Wu, Tau lepton asymmetry by sterile neutrino emission—Moving beyond one-zone supernova models, J. Cosmol. Astropart. Phys. 12 (2019) 019.
[86] Sherwood Richers and Manibrata Sen, Fast flavor transformations, arXiv:2207.03561.
[87] Shashank Shalgar and Irene Tamborra, Supernova neutrino decoupling is altered by flavor conversion, arXiv:2206.00676.
[88] Hiroki Nagakura and Masamichi Zaizen, Time-dependent, quasi-steady, and global features of fast neutrino-flavor conversion, arXiv:2206.04097.
[89] Shashank Shalgar and Irene Tamborra, Neutrino flavor conversion, advection, and collisions: The full solution, arXiv:2207.04058.
[90] Günther Sigl and Georg G. Raffelt, General kinetic description of relativistic mixed neutrinos, Nucl. Phys. **B406**, 423 (1993).
[91] S. P. Mikheev and A. Yu. Smirnov, Neutrino oscillations in a variable density medium and neutrino bursts due to the gravitational collapse of stars, Sov. Phys. JETP **64**, 4 (1986).
[92] L. Wolfenstein, Neutrino oscillations in matter, Phys. Rev. D **17**, 2369 (1978).
[93] S. P. Mikheev and A. Y. Smirnov, Resonance enhancement of oscillations in matter and solar neutrino spectroscopy, Sov. J. Nucl. Phys. **42** (1985), https://www.osti.gov/biblio/5714592.
[94] C. W. Kim, Jewan Kim, and W. K. Sze, On the geometrical representation of neutrino oscillations in vacuum and matter, Phys. Rev. D **37**, 1072 (1988).
[95] Stephen J. Parke, Nonadiabatic Level Crossing in Resonant Neutrino Oscillations, Phys. Rev. Lett. **57**, 1275 (1986).
[96] Mattias Blennow and Alexei Yu. Smirnov, Neutrino propagation in matter, Adv. High Energy Phys. **2013**, 972485 (2013).
[97] Georg G. Raffelt and Günther Sigl, Neutrino flavor conversion in a supernova core, Astropart. Phys. **1**, 165 (1993).